Fuel 429 (2027) 140854

Contents lists available at ScienceDirect

Fuel

journal homepage: www.elsevier.com/locate/fuel

Full Length Article

Optimizing prechamber design and engine calibration for non-quiescent lean-burn gas engines through 0/1D predictive combustion and emissions models

Andrea Piano [a,*], Guglielmo Rossi [a], Federico Millo [a], Enrica Malfi [b], Vincenzo De Bellis [b], Francesco Lassandro [c], Alessandro Cimarello [c], Jari Hyvönen [d], Alberto Cafari [d]

[a] Politecnico di Torino, Energy Department, Italy
[b] Università di Napoli "Federico II", Italy
[c] Wärtsilä Italia S.p.A., Italy
[d] Wärtsilä Finland OY, Finland

ABSTRACT

Lean-burn gas operation is essential for meeting strict nitrogen oxides (NOx) emissions regulations and reducing fuel consumption in marine and power generation engines. Because efficient lean combustion requires high-energy ignition sources, the active Pre-Combustion Chamber (PCC) is universally recognized as the optimal solution for large-bore applications. To accelerate engine development and drastically reduce experimental burdens, accurately modelling these complex combustion dynamics using computationally efficient Zero/One-Dimensional (0D/1D) predictive tools is now a critical requirement.

To address this challenge, this study presents a comprehensive 0D/1D predictive simulation platform developed in GT-SUITE, tailored to co-optimize PCC geometry, in-cylinder flow motion, and engine calibration for lean-burn gas engines.

The framework integrates advanced phenomenological models for predictive combustion, as well as for NOx and unburnt hydrocarbons (HC) emissions. Its predictive capabilities were rigorously validated against an extensive experimental dataset encompassing two distinct pre-chamber designs, demonstrating excellent agreement. Furthermore, the inclusion of a 0D turbulence model guaranteed high-fidelity resolution of flow-combustion interactions, enabling the precise analysis of both quiescent and non-quiescent combustion systems.

Serving as a highly efficient computational alternative to demanding Three-Dimensional Computational Fluid Dynamics (3D-CFD) campaigns, the validated framework was leveraged to systematically determine the optimal synergistic configuration of PCC architecture, in-cylinder flow motion, and engine calibration. The optimization analysis demonstrated that the configuration obtained for swirl motion provided the greatest overall benefits, delivering a +1.6% increase in indicated thermal efficiency at full load and minimized unburned HC emissions by -600 ppm at low load.

1. Introduction

Natural gas has been increasingly used as a primary fuel in a variety of energy sectors, including marine propulsion [1] and power generation [23], as a result of stricter regulations aimed at reducing greenhouse gas and pollutant emissions over the coming decades.

Specifically, because of its favourable hydrogen-to-carbon ratio [4], natural gas combustion results in lower Carbon Dioxide (CO_2) emissions per energy unit compared to diesel oil. Furthermore, in the context of the transition toward carbon-neutral fuels, fossil-derived natural gas is projected to be progressively replaced by synthetic gas derived from biomass or renewable energy sources [5]. This shift will significantly lower the carbon footprint of these energy sectors while simultaneously making use of existing technologies and infrastructure. Consequently, Internal Combustion Engines (ICEs) fuelled with natural gas are expected to be crucial in future power generation scenarios in which renewables will dominate.

Thanks to lean-burn combustion, natural gas has the potential to reduce Nitrogen Oxides (NOx) emissions in ICEs by 80-85% compared to heavy fuel oil. Moreover, sulphur oxides emissions are almost eliminated as natural gas does not contain sulphur, while particulate matter production is very low [1]. Unfortunately, the main drawback of lean operation is that it increases Unburnt Hydrocarbons (HC) emissions with respect to stoichiometric operation, especially at low load [6,7].

In the realm of large-bore natural gas engines, the lean-burn concept [8], combined with innovative ignition systems [9], currently stands as

* Corresponding author.
E-mail address: andrea.piano@polito.it (A. Piano).

https://doi.org/10.1016/j.fuel.2026.140854
Received 28 April 2026; Received in revised form 30 June 2026; Accepted 30 July 2026
Available online 3 August 2026

the primary strategy to balance high engine efficiency with combustion stability. While increasing the air-to-fuel ratio promotes a highly efficient combustion process, it simultaneously tends to worsen cycle-to-cycle variability when conventional spark plug ignition is employed [10]. In this context, the Pre-Combustion Chamber (PCC) ignition system offers a viable solution [1112] to overcome this problem.

Specifically, the PCC consists of a small ignition volume situated within the cylinder head and equipped with a conventional spark plug and connected to the Main Chamber (MC) via small orifices. PCC can also be supplied by a dedicated fuel line (i.e., active PCC). The combustion of a near-stoichiometric mixture within the PCC generates highly reactive, turbulent jets [13], which are projected into the MC. These jets work as distributed, multiple ignition sites that feature a significantly higher energy than a single spark [14]. This mechanism provides substantial improvements in combustion stability [15], thereby ensuring a robust combustion process even with lean mixtures. Commonly, the ignition mechanism is named Turbulent Jet Ignition (TJI) if the ignition of the main charge is induced by the self-ignition of highly reactive turbulent jets coming out of the PCC. On the other hand, if the flame can propagate through the PCC holes reaching the MC without being quenched, the ignition mechanism is usually referred to as the torch ignition system [16]. Large-bore engines typically employ large orifices (diameter > 2 mm), thereby favouring torch ignition [17].

In order to optimize the combustion process [18], not only in terms of indicated efficiency but also concerning NOx and HC emissions [19], a proper PCC design becomes crucial. Its geometry (shape, volume, nozzle orientation), the nozzle hole diameter, and the number of nozzle holes are the design parameters that have to be optimized. For instance, the nozzle hole diameter influences the timing of hot jet ejection into the MC and the establishment of the pressure difference between the PCC and MC [20]: a smaller diameter can lead to a faster jet velocity and a higher jet intensity, influencing the combustion duration in the MC [21]. Moreover, an increase in PCC volume can help in reducing the MC combustion duration [22]. The number of nozzle holes should be properly designed to avoid significant unburnt gaps between the hot flame jets [23].

Because the design of these architectures involves multiple degrees of freedom, relying on traditional experimental campaigns would be prohibitively time-consuming and costly. Consequently, numerical simulations have become indispensable for accelerating engine development and calibration. By effectively bypassing the need for exhaustive physical testing, these predictive computational tools drastically streamline the engine development and optimization process, significantly reducing the overall time-to-market.

Three-Dimensional Computational Fluid Dynamics (3D-CFD) simulations can be exploited to investigate how the PCC design can influence the combustion process (e.g., combustion within the PCC, jet development, and ignition behaviour in the MC) [24,25]. Thanks to these, Liu et al. found out that in-cylinder flow motions can improve combustion quality. Swirl and tumble, indeed, can accelerate the mixing process of natural gas with air and thus the propagation of the flame [26], resulting in higher combustion efficiency and lower pollutant emissions [27].

For a faster optimization in terms of computational time, Zero-Dimensional/One-Dimensional Computational Fluid Dynamics (0D/1D-CFD) numerical models can be exploited to obtain less detailed but still reliable estimates of the overall engine system performance, especially in the early stage of the development process of the engine, and also during its calibration process. Given the physical complexity of this combustion system, developing reliable 0D/1D predictive models represents a significant challenge. To be effective, the framework must accurately capture how PCC geometry and in-cylinder flow kinematics dictate the overall combustion process and pollutant formation.

To this end, different 0D/1D combustion models have been developed and validated: Zhu et al. developed and validated a parameter-based double-Wiebe model [28] for a PCC-ignited large-bore single-cylinder engine; Bozza et al. developed and validated a phenomenological combustion and pollutant emissions model for PCC engines [29]. In line with the aforementioned research activities, the commercially available software GT-SUITE incorporates a fully predictive phenomenological model for the combustion process simulation in PCC engines [30]. Accurso et al. successfully demonstrated the reliability of this model for lean-burn, large-bore natural gas PCC engines [31].

To accelerate the development, design optimization, and calibration of lean-burn gas engines with either quiescent or non-quiescent combustion systems, this study develops a comprehensive 0D/1D-CFD predictive simulation platform within GT-SUITE. Equipped with a fully predictive combustion model, a dedicated turbulence model, and advanced NOx and HC emission sub-models, the platform allows for the simultaneous co-optimization of PCC architecture, in-cylinder flow dynamics, and engine calibration. Its high sensitivity to hardware and calibration variations ensures robust system-level analysis, acting as a computationally faster design alternative to traditional 3D-CFD simulations.

Ultimately, the proposed platform overcomes the inherent complexity of PCC-MC combustion systems, drastically cutting the reliance on physical test-bench campaigns. This not only drastically reduces time-to-market and development costs but also significantly minimizes the carbon footprint of the engineering process. Crucially, to the best of the authors' knowledge, this study pioneers the use of a fully predictive 0D/1D framework to co-optimize the combustion system of lean-burn gas engines. By explicitly resolving the complex interplay between PCC geometry and in-cylinder flow dynamics, this work establishes a highly effective methodology to maximize thermal efficiency and reduce pollutant emissions.

2. Case Study

In this work, the Wärtsilä W6L46TS-SG was selected as the case study. Its main technical specifications are listed in Table 1.

The engine under investigation is a four-stroke six-cylinder natural gas engine, equipped with active PCCs. Operating with a near-stoichiometric air-fuel mixture, combustion in the PCC exhibits rapid flame propagation, resulting in a sharp pressure increase immediately after spark ignition. This sudden rise in pressure expels hot flame jets from the PCC into the MC. Due to the relatively large nozzle diameter ($>$ 4 mm), these jets do not undergo quenching during the transfer, allowing them to successfully ignite the lean mixture within the MC.

The available experimental dataset used to calibrate and validate the combustion and emission models was comprehensive of about 100 operating points, including load sweeps, ignition timing sweeps, boost pressure variations, and PCC gas injection sweeps (start of injection and injection duration).

During the experimental campaign, steady-state performance parameters – namely, air flow rate, natural gas consumption, and exhaust emissions – were recorded for each test point alongside high-frequency, crank-angle-resolved in-cylinder pressure measurements. The steady-state quantities were acquired using low-frequency measurement systems. Detailed specifications of the instrumentation, including their respective measurement accuracies, are summarized in Table 2.

The acquired operating points spanned two different PCC

Table 1
Wärtsilä W6L46TS-SG engine technical specifications

Specification	Unit	Value
Number of cylinders	–	6
Turbocharger	–	Dual stage with wastegate
Bore	mm	460
Stroke	mm	580
Engine Speed	RPM	600
Maximum Power	kW	7800

Table 2
Instrumentation accuracy.

Variable	Instrument	Accuracy
In-cylinder pressure	Kistler transducer	0.2 %
Air flow rate	Orifice flowmeter	0.9%
Natural gas consumption	Coriolis type flowmeter	0.35%
Exhaust gas emissions	Horiba Mexa-One (NOx, CO, HC, CO_2, O_2)	1%

geometries, depicted in Fig. 1.

- **PCC #1**: it features a mixing volume connected to the PCC holes through a connecting duct with a lower diameter; the spark plug and the gas admission pipe are located on top of the mixing volume.
- **PCC #2**: same design as PCC#1, but it features an increased diameter of the PCC nozzle holes (+20%) and an increased diameter of the connecting duct (+15%). The total volume of the PCC is slightly larger.

The highlighted geometrical differences between PCC #1 and PCC #2 directly influence flame propagation. To rigorously assess the model's reliability and its sensitivity to such geometric variations, a cross-validation approach was adopted: the calibration was performed exclusively on PCC #1, while PCC #2 was employed for validation, effectively proving the model's predictive capability across different designs.

3. Simulation Platform

The developed GT-SUITE engine model comprises the entire engine architecture, including both the PCC and the MC. Specifically, the *SITurb* combustion model was used to simulate the flame propagation within the PCC, while the *JetIgnition* model was used in the MC. These models were specifically tailored for this case study, with a focus on customizing the laminar and turbulent flame speed models. All the turbulence-related quantities required by the combustion models were evaluated via the *K-k-ε* phenomenological 0D model. Concerning the emissions, a stratified burned zone formulation was adopted for the prediction of NOx emissions through the Zeldovich kinetic model, while a specifically customized HC emissions model was implemented.

The following subsections provide a more detailed discussion of the specific models employed in this study.

3.1. Combustion model

The combustion processes in both the PCC and MC were resolved using phenomenological, predictive multi-zone models specifically tailored for this research. To capture these phenomena, the *SITurb* model was applied to predict flame propagation within the PCC, while the *JetIgnition* model was employed to predict combustion in the MC.

The reliability of the *SITurb* model is well-documented in the literature, having been effectively applied to simulate both gasoline engines [32,33] and hydrogen combustion processes [34]. Adopting a two-zone approach, the *SITurb* model describes the evolution of a spark-ignited turbulent flame. Specifically, the unburned mixture is progressively entrained by the advancing flame front, and it is subsequently burned behind it. The rate of this mass entrainment is modelled as directly proportional to the turbulent flame speed, according to Eq. (1):

$$\frac{dM_e}{dt} = \rho_u A_f (S_T + S_L) \tag{1}$$

where M_e designates the mass of the entrained unburned mixture, A_f stands for the flame front area, ρ_u is the unburned mixture density, while S_T and S_L are the turbulent and laminar flame speeds, respectively. The flame area is initially computed under the assumption of a hemispherical propagation. The burn rate is computed according to Eq. (2):

$$\frac{dM_b}{dt} = \frac{M_e - M_b}{\tau} \tag{2}$$

where τ represents the time required for the flame to propagate across the turbulent Taylor microscale (λ) at the laminar flame speed, as defined in Eq. (3).

$$\tau = \frac{\lambda}{S_L} = C_{TLS,PCC} \frac{L_i}{\sqrt{Re_t}} \frac{1}{S_L} \tag{3}$$

where L_i is the turbulence integral length scale, Re_t represents the turbulent Reynolds number, and $C_{TLS,PCC}$ serves as a tuning constant. A detailed description of the models employed to evaluate the laminar and turbulent flame speeds will be provided later in the manuscript.

The *JetIgnition* model simulates the MC combustion process by superimposing jet-driven and flame-propagation contributions. During the simulation, the cylinder is discretized into three interacting thermodynamic zones: the *Main Unburned Zone* (fresh air and port-injected natural gas); the *Jet Zone* (the discharging PCC jets and entrained mass, computed via momentum conservation); and the *Burned Zone*, where burned gases accumulate based on the jet and turbulent flame burn rates.

The jet penetration S is computed according to Eq. (4), where t is the elapsed time and u_n denotes the velocity at the prechamber nozzle. d_n and C_d are the hole diameter and its related discharge coefficient, ρ_n and ρ_{cyl} represent the fluid density at the nozzle exit and inside the main chamber, respectively, and C_s is a model constant.

$$S(t) = C_s t^{0.5} \left(\frac{u_n d_n}{C_d} \sqrt{\frac{\rho_n}{\rho_{cyl}}} \right)^{0.5} \tag{4}$$

The mass entrained into the jet, m_{je}, is computed assuming momentum conservation during jet penetration, as expressed by Eq. (5):

$$m_{je} = C_e m_n \left(\frac{u_n}{u(t)} - 1 \right) \tag{5}$$

where m_n is the mass of the jets at the prechamber nozzle exit, and C_e is a calibration constant.

The ignition delay is evaluated based on the thermodynamic conditions within the jet using an Arrhenius-type formulation. In the jet region, the burn rate is calculated as follows:

$$\frac{dm_{jb}}{dt} = C_{diff} m_{ju} \frac{\sqrt{TKE}}{V_{cyl}^{1/3}} f(x_{O_2}) + \dot{s}_f m_{ju} \tag{6}$$

In this equation, m_{jb} and m_{ju} denote the burned and unburned masses within the jet region, respectively. *TKE* represents the turbulent kinetic energy, V_{cyl} is the cylinder volume, and C_{diff} serves as a tuning constant. The ratio $\sqrt{TKE}/V_{cyl}^{1/3}$ defines a mixing-controlled burning rate – as proposed by Magnussen [35] – which is governed by the in-cylinder turbulence level and local jet properties. Additionally, $\dot{s}_f$ acts as a source term coupling the combustion within the *Jet Zone* to that

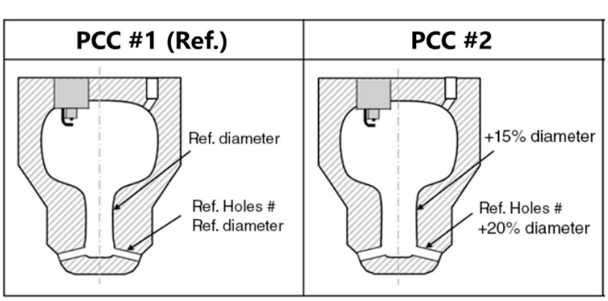

Fig. 1. Pictorial representation of the PCCs internal geometry.

occurring behind the primary flame front.

For the flame propagation component, the model adopts the same two-zone entrainment-burn approach used in the PCC. Like $\dot{s}_f$ (Eq. (6)), an additional source term, $\dot{s}_j$, is introduced to compute the burn rate of the mass entrained by the flame in the MC. This term couples the combustion behind the flame front with the combustion within the jets, as expressed in Eq. (7):

$$\frac{dm_{fb}}{dt} = \frac{m_{fe} - m_{fb}}{\tau} + \dot{s}_j m_{fb} \tag{7}$$

where m_{fb} represents the burned mass originating from flame combustion, $m_{fe} - m_{fb}$ indicates the instantaneous unburned mass entrained into the flame front, and τ denotes the Taylor length scale. The source terms $\dot{s}_f$ and $\dot{s}_j$ (utilized in Eq. (6) and (7)) take into account that the unburned mass entrained but not yet burned by the jet remains available for consumption behind the main flame, and vice versa. Moreover, the transition from jet autoignition to physical flame propagation is simulated via a transition function, employing a methodology similar to Walther et al. [36].

Governed by this function, the modelled flame surface evolves linearly from the initial jet geometry, defined as a truncated cone ending in a hemisphere, to the spherical shape characteristic of flame propagation in the MC.

A more detailed description of the model can be found in [30,37].

As previously introduced, the combustion models were specifically tailored for this case study, with a focus on the laminar and turbulent flame speed models.

This engine operates with lambda values higher than 2, very high peak pressures, and relatively low temperatures due to the strong Miller level. Therefore, a dedicated modelling approach is required, as standard formulations of laminar flame speed found in the literature are typically optimized for lower pressures and near-stoichiometric conditions, as highlighted in [38].

Moreover, the combustion processes in the PCC and the MC are characterized by significant differences in mixture composition. While the MC contains a lean mixture with a very low residual gas fraction, the active PCC typically operates with a richer mixture, characterized by a near-stoichiometric air-fuel ratio and containing a significant amount of burned gases from the previous engine cycle.

For these reasons, a tabulated laminar flame speed approach was adopted. The laminar flame speed values, evaluated by means of detailed chemistry calculations [39], were interpolated from look-up tables based on the instantaneous conditions in the MC and PCC. These values were determined as a function of pressure, temperature, equivalence ratio, and residual gas fraction, and were subsequently given as an input to the *SITurb* and *JetIgnition* combustion models, accounting for the differences in mixture composition in PCC and MC.

Concerning the turbulent flame speed model, the Kobayashi correlation [40] was adopted for the MC. This model has been demonstrated to accurately describe the flame velocity of lean methane-air mixtures, as reported in [38].

3.2. Turbulence model

The predictive capability of both *SITurb* and *JetIgnition* relies on the precise determination of turbulent intensity and turbulent length scale within the PCC and the MC, respectively. For this reason, these turbulence-related quantities are computed using a phenomenological 0D turbulence model [41].

The 0D turbulence model, based on the K-k-ε approach, was specifically calibrated for the MC and PCC (PCC #1 configuration) against cold-flow 3D-CFD simulation results obtained using a Reynolds-Averaged Navier-Stokes (RANS) k-ε turbulence model. A comparison between the volume-averaged 3D-CFD data and the predicted 0D results is reported in [31].

Moreover, the 0D turbulence model captures the geometric influence of intake ports and valves, thereby ensuring an accurate prediction of turbulence levels for both quiescent and non-quiescent combustion systems. To robustly capture large-scale flow structures, the modelling of swirl and tumble motions is governed by two sets of coefficients – namely, the swirl coefficient and the tumble coefficient – which were obtained via dedicated 3D-CFD flow bench simulations.

3.3. NOx emissions model

In the present study, the formation of NOx emissions in the cylinder is predicted using the Zeldovich kinetic model [42]. Reliable NOx predictions rely heavily on the accurate estimation of the temperature distribution within the burned gas zone. Specifically, the burned gases that are produced in the early phase of the combustion process undergo a further compression, reaching temperatures significantly higher than those attained immediately after combustion. This thermal stratification has a significant impact on the levels of NOx produced. For this reason, in this case study, a multi-zone NOx emissions model was implemented both in MC and PCC.

In such a model, the in-cylinder burned zone is discretized into 10 thermodynamic sub-zones. These sub-zones receive mass from the unburned region and can exchange heat with the cylinder walls. Moreover, the combustion process is divided into 10 unequal subsections of mass fraction burned, where a finer resolution is allocated to the early combustion phase. Mass from the unburned zone is transferred to the active sub-zones during their respective combustion interval. Consequently, as mass is added to the current sub-zone, the previously formed sub-zones are progressively compressed, resulting in a local temperature rise. The Zeldovich NOx kinetics are evaluated within each sub-zone based on the local temperature. The total NOx emitted during combustion is then calculated as the cumulative sum of the NOx produced in each zone. Further details can be found in [38].

3.4. HC model

A dedicated HC emissions model has been developed and implemented. The HC model captures HC formation through two principal mechanisms: mass exchange with the piston top-land crevice, modelled as a filling/emptying process [43], and flame wall quenching [44]. Crevice dynamics were resolved by applying coupled mass, species, and energy conservation within the top-land volume, providing crank-angle–dependent estimates of the local pressure and temperature in line with the approach reported in [45,46,47,48]. Wall quenching was described by considering flame extinction at the chamber surfaces. As is known, this is driven by heat transfer losses, which leave a near-wall layer of unburned mixture during flame propagation, contributing to total HC output. The thickness of this quenched layer, δ_q, was linked to the flame thickness, δ_f, via the Peclet-number, which was evaluated using the correlation proposed in [44], as summarised in Eq. (8).

$$\left(\frac{\delta_q}{\delta_f}\right) = Pe_q = \frac{(T_f - T_w)}{(T_f - T_u)} \cdot \frac{c_q}{\phi_q} \tag{8}$$

In Eq. (8), the temperatures T_f, T_u, and T_w correspond to the adiabatic flame temperature, the unburned-mixture temperature, and the wall temperature, respectively. The parameter ϕ_q quantifies the fraction of the chemical heat release that is transferred to the walls within the flame zone, normalised by the total heat released by fuel oxidation. The correlation in [44] was originally derived for stoichiometric gasoline/air flames and assumed $\phi_q = 0.3$. To address the observed deviations of the correlation in case of different fuels and near-wall thermal regime, Eq. (8) is augmented with a calibration constant c_q.

The HC mass formed through the mechanisms described above was assumed to undergo post-oxidation before exhaust. To more accurately represent the thermodynamic conditions and local mixture composition governing this stage, a boundary-layer modelling strategy was adopted. This framework, validated against 3D-CFD results in [47], was found to improve prediction accuracy relative to the standard post-oxidation formulations commonly followed in the literature [49,50]. The approach solves coupled mass and energy conservation equations over a near-wall control region of the cylinder in which post-oxidation is presumed to occur. The post-oxidation rate was modelled with a single-step global kinetic expression (Eq. (9)).

$$\frac{d[HC]}{dt} = -A\cdot[HC]^{\alpha}\cdot[O_2]^{\beta}\cdot exp\left(-\frac{E}{R\cdot T}\right) \tag{9}$$

The parameters of Eq. (9) are tuned to methane/air chemistry according to [51] and are listed in Table 3.

After applying the post-oxidation reduction, the HC contributions associated with each formation source were summed and then imposed as the HC concentration at the exhaust valve during the gas-exchange process

3.5. Model calibration & validation

As mentioned above, the models were calibrated relying solely on experimental data from one specific PCC geometry (PCC #1). Their predictive accuracy was subsequently validated against the second architecture (PCC #2), demonstrating a strong agreement between predicted and experimental combustion results, as illustrated by the correlation plots in Fig. 2. It is worth to point out that a single set of calibration constants was used across the entire dataset, thereby confirming the model's sensitivity to PCC design changes and its ability to reproduce the resulting combustion characteristics.

The current simulation framework relies on specific fluid-dynamic and thermal simplifications that, as demonstrated by the results, did not compromise its overall predictive accuracy. On the combustion side, although the model does not explicitly resolve localized jet-induced turbulence and lacks a direct geometric distinction between turbulent and torch ignition regimes, proper tuning of the calibration constants allows it to specifically reproduce the torch ignition behaviour. This ensures the model successfully captures the pre-chamber geometry dependency. Conversely, on the thermal side, the temperature evolution of the pre-chamber is not modelled. In practice, a reduction in pre-chamber permeability, resulting from a smaller volume, can enhance overall heat transfer, physically leading to an increased PCC tip temperature and subsequent hot spots for mixture ignition. This specific thermal phenomenon is therefore neglected. Despite these simplifications, the model maintains robust predictive capabilities and achieves highly accurate results.

Fig. 3 compares the experimental and predicted traces for PCC pressure, MC pressure, and MC heat release rate (HRR) at 100%, 50%, and 25% load. These operating points served as the baseline for the subsequent PCC geometry and flow motion optimization. As observed, the model demonstrates excellent agreement with the experimental data.

Building upon the successful validation of the combustion model, the emissions models similarly exhibit robust predictive capabilities. Fig. 4 (a) and Fig. 4(b) depict the predicted versus experimental NOx and HC emissions during a lambda sweep and a spark advance sweep at 50% load, respectively. The calibrated models successfully capture the experimental trends for both pollutants, underscoring their reliability for the subsequent optimization phase.

Table 3
Post-oxidation rate parameters [51]

Parameter	Value
A	1.30 × 108
α	-0.3
β	1.3
E_a	48.4

Table 4 summarizes the absolute Root Mean Square Error (RMSE) values for the combustion and the emissions models, providing a comprehensive quantitative assessment of the model's predictive performance across the full experimental dataset.

The consistent, high-fidelity agreement observed between the experimental and predicted results effectively validates the implemented models. Thus, the simulation platform can be confidently deployed for the subsequent design of PCC geometries and the comparative analysis of different in-cylinder flow motions.

Although some discrepancies can be observed in absolute terms, the model reliability was deemed sufficient to proceed with the subsequent optimization analysis. As demonstrated by the combustion and emissions model results (in Fig. 2, Fig. 3, and Fig. 4, respectively), the models are capable of accurately capturing the observed trends from both qualitative and quantitative perspectives. Therefore, variations in geometry and calibration can be effectively accounted for within the developed platform, ensuring robustness in the optimization process.

4. Optimization Methodology

Once the simulation platform was validated against experimental data, it was used to determine the optimal configuration of PCC design, flow motion, and engine calibration. This section outlines the adopted optimization methodology, which focuses on maximizing Indicated Thermal Efficiency (ITE) and minimizing HC emissions, while keeping NOx emissions equal to or lower than the baseline case.

4.1. Design space definition

In this study, 60 different PCC configurations were simulated, combining variations in PCC volume, number of nozzle holes, and nozzle hole diameter. These combinations resulted in a nozzle Area-to-Volume ratio (A/V, defined as the ratio of total area of nozzle holes to the PCC volume) ranging from –50% to +260% compared to the baseline PCC#1 design detailed in Section 2 and Fig. 1. Adopting PCC#1 as the reference geometry (REF), the characteristics of all 60 tested configurations are expressed as relative deviations in volume, hole count, and hole diameter. The complete parametric matrix of these designs is provided in Table 5.

All the configurations were tested using a full-factorial Design of Experiments (DoE) approach. This comprehensive analysis was made feasible by the high computational efficiency featured by the developed simulation platform.

The optimization framework investigated three distinct intake port designs, each generating a specific in-cylinder flow motion: quiescent, tumble, and swirl. The modelling of the in-cylinder kinematics is governed by the intake valves swirl and tumble coefficients, defined as the ratio of the angular momentum flux to the linear momentum flux across the intake valves. Together with the valves discharge coefficient, these parameters directly influence the turbulence quantities predicted by the 0D K-k-ε turbulence model within the MC, thereby capturing the full impact of the intake port design on the flow field, and subsequently, its influence on the combustion process. Therefore, the specific swirl and tumble coefficients for each configuration were extracted from dedicated 3D-CFD virtual flow bench analyses and integrated into the simulation platform. For the sake of brevity, a detailed discussion of the 3D-CFD methodology is omitted from this manuscript.

Fig. 5 shows the swirl and tumble coefficients as a function of valve Lift over Diameter ratio (L/D) for the three configurations under study. The swirl coefficient values of the three flow motions are normalized by the maximum value observed in the swirl case, while the tumble coefficient is normalized by the peak value of the tumble case. Similarly, L/D is normalized by its maximum value.

The design optimization was performed at three distinct load levels (100%, 50%, and 25%, as depicted in Fig. 3) to assess the influence of

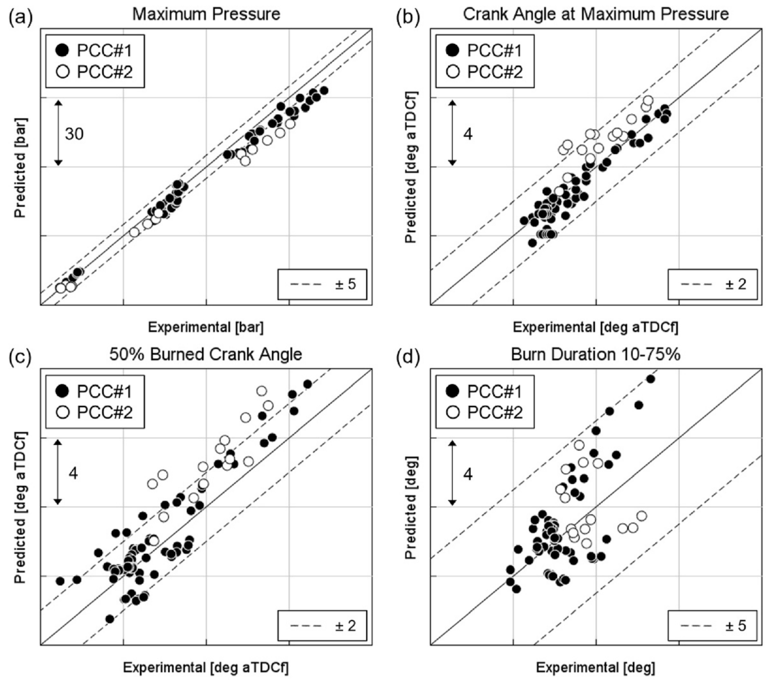

Fig. 2. Correlation plots between experimental and predicted combustion results: maximum MC pressure (a), crank angle at maximum MC pressure (b), 50% burned crank angle (c), burn duration 10-75% (d). PCC #1 in black, PCC #2 in white.

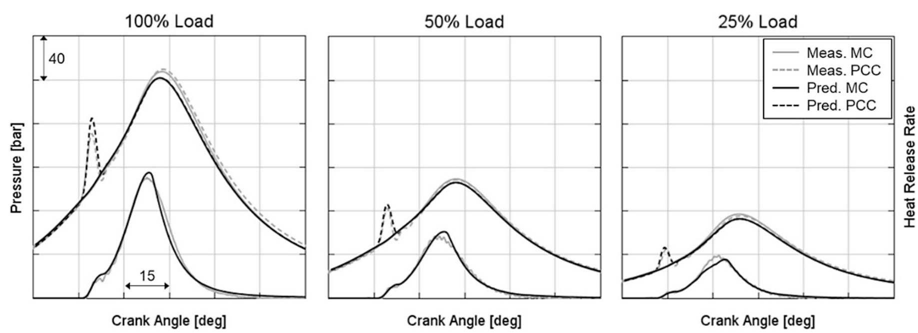

Fig. 3. Experimental and simulation comparison in terms of MC pressure, PCC pressure, and MC HRR over a load variation from 100% to 25%.

the proposed design changes across the entire engine map. Specifically, the objective was to verify the potential for ITE gains at high load and a reduction of HC emissions at low load, which represents the most critical operating condition for HC emissions.

The optimization methodology was divided into two distinct steps. The first one defined the optimal coupling between PCC geometry and in-cylinder flow motion using the baseline engine calibration. The second step identified the necessary calibration refinements – specifically in terms of air-to-fuel ratio and spark advance – for the selected hardware configuration.

In all these steps, the study was conducted maintaining a lambda value equal to 1 within the PCC for all simulated designs. This approach was adopted to exclude any influence that the change in geometry or flow motion can have on the fuel-air mixture formation inside the PCC.

4.2. Definition of the optimal PCC and flow motion combination

The first step of the optimization focused on identifying the optimal coupling between the PCC geometry and in-cylinder flow motion under baseline engine calibration conditions.

Fig. 6 illustrates an example of the DoE methodology applied to identify the optimal design for the quiescent flow motion case with the REF number of nozzle holes. Similar analyses, not detailed here for sake of brevity, were conducted for engine variants featuring swirl and tumble flow motions, as well as varying the number of nozzle holes. The results, in terms of maximum MC pressure (a), NOx emissions (b), indicated efficiency (c), and HC emissions (d), are plotted as a function of nozzle hole diameter and PCC volume.

In this case, the reduction of the PCC volume led to a reduction in both the maximum MC pressure and NOx emissions, combined with a decrease in ITE and an increase in HC levels. First, since the PCC mixture is stoichiometric, a smaller PCC volume inherently reduces the NOx mass formed within the PCC itself. Second, this reduced fuel mass translates to a lower thermal energy delivered by the ignition jets. This energy deficit reduces the combustion intensity in the MC, thereby further suppressing overall NOx formation while concurrently explaining the aforementioned penalties in peak MC pressure, ITE, and HC.

These results align with the findings of Shah et al. [22], who experimentally demonstrated that NOx emissions decreased for smaller PCC volumes. This trend occurred alongside a reduction in MC combustion intensity, which ultimately translated into a lower lean limit for smaller PCCs.

On the other hand, reducing the nozzle hole diameter increased both the maximum MC pressure and ITE, while reducing HC levels. This result

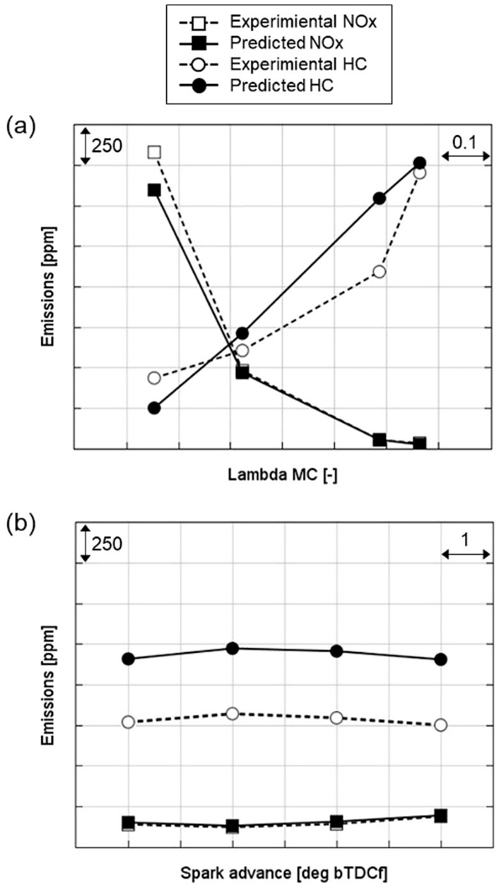

Fig. 4. Comparison between experimental and predicted NOx and HC emissions results: (a) MC lambda sweep at 50% load operating condition, (b) spark advance sweep at 50% load operating condition.

Table 4
Combustion and emissions models RMSEs.

Parameter	RMSE	R^2
Peak pressure MC	4.9 bar	98.5%
CA at peak pressure MC	0.9 deg	80.0%
CA at 50% burned fuel MC	1.8 deg	74.5%
Burn duration 10-75 MC	2.5 deg	18.6%
NOx emissions	150 ppm	96.4%
HC emissions	416 ppmC1	41.0%

Table 5
Different PCC geometries tested

Hole diameter	REF -28%; REF -18%; REF -6%; REF+4%
Number of holes	REF -1; REF; REF +1
Volume	REF -65%; REF -48%; REF -30%; REF+15%; REF

is driven by a higher jet velocity from the PCC, which promotes a faster combustion in the MC. These findings are confirmed by the experiments of Gentz et al. [21], who identified that under lean conditions, smaller nozzle hole diameters result in faster, more vigorous jets, thereby enhancing MC combustion.

Concerning NOx, the results reveal a non-monotonic trend, indicating that NOx formation is governed by the balance between the higher PCC combustion intensity, generated by a reduced nozzle hole diameter, and the modified MC combustion resulting from the higher velocity jets.

As shown by the two shaded regions in Fig. 6, the selection of the optimal PCC geometry is subject to two primary constraints. On one hand, the maximum MC pressure must remain below the baseline level to respect the mechanical limits of the engine. On the other hand, NOx emissions must be kept at or below the baseline value to meet emissions limits.

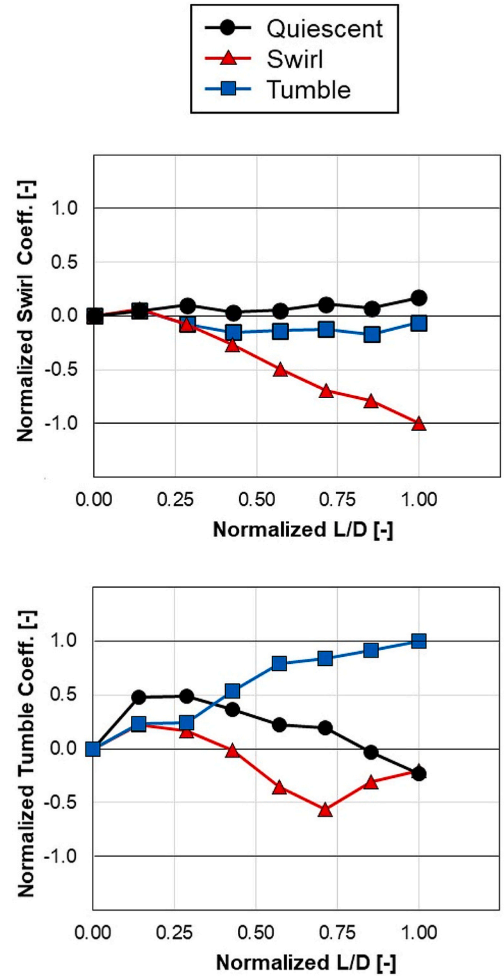

Fig. 5. Normalized swirl and tumble coefficients vs normalized valve lift over diameter ratio

The optimal design was identified by analysing the ITE map. Within the remaining compliant map, the candidate with the highest ITE was selected. Although this specific case showed a slight ITE penalty (-0.1%), it offered a valuable advantage in terms of NOx emissions reduction. Specifically, the configuration with a 30% reduction in PCC volume and a 28% reduction in nozzle hole diameter yielded a NOx decrease of 41.8 ppm. This NOx margin provided the opportunity to enrich the fuel-air mixture, thereby restoring NOx to the baseline level while simultaneously increasing ITE, as discussed in the following subsection.

Regarding HC emissions, the observed value was slightly higher than the baseline (+32.7 ppm), an increase that can be attributed to the minor loss in efficiency. This increase was then compensated in the following optimization step by reducing lambda, thereby increasing ITE and lowering HC emissions.

Through this selection approach, the best PCC geometry was chosen for every flow motion under study.

4.3. Definition of the optimal engine calibration

The second step of the optimization focused on the calibration refinements in terms of air-to-fuel ratio and spark advance for the optimal combination of PCC design and flow motion found in the previous step.

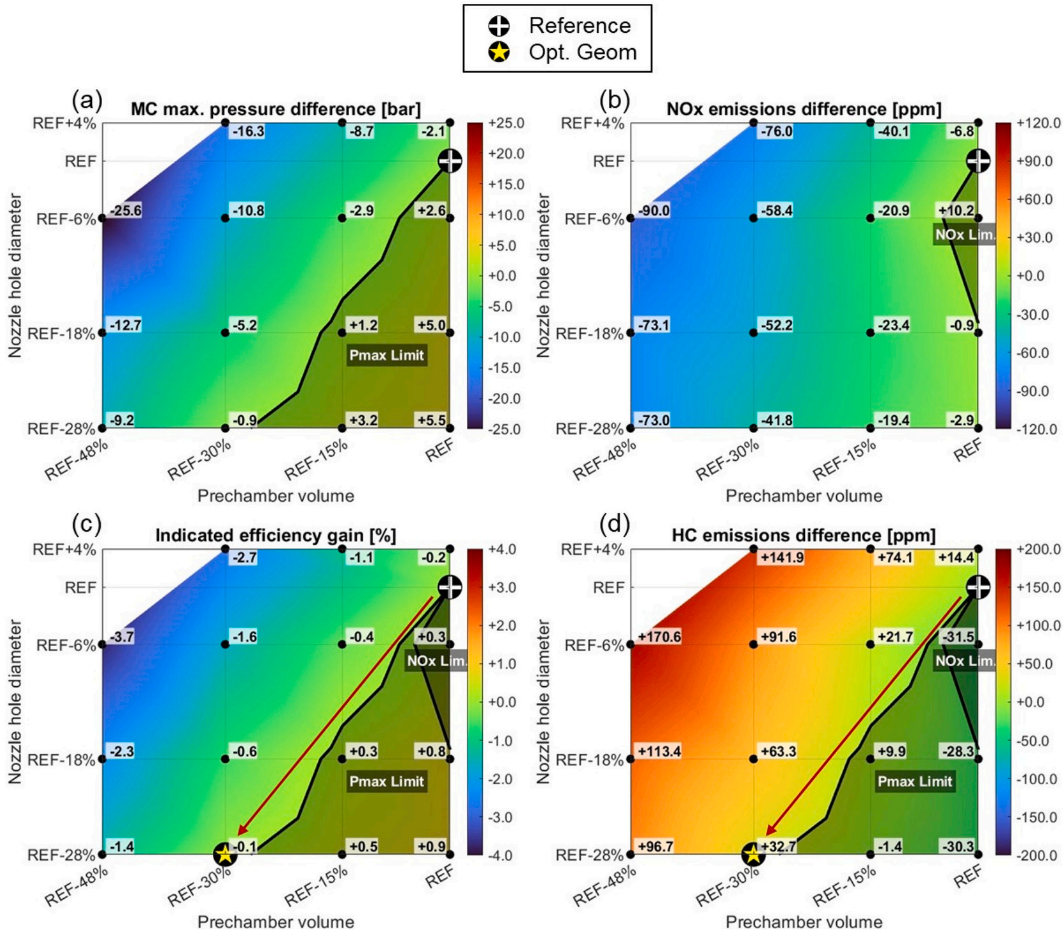

Fig. 6. PCC optimal geometry selection for quiescent flow, REF number of nozzle holes and 100% Load: (a) Maximum MC pressure, (b) NOx emissions, (c) ITE, (d) HC emissions.

A similar DoE approach was adopted to select the optimal engine calibration, as shown in Fig. 7. This figure shows, as an illustrative example, the results for the quiescent-flow case with the REF number of nozzle holes.

As in the previous step, the calibration must be constrained to avoid exceeding the baseline maximum MC pressure while maintaining NOx emissions at or below the baseline level. Based on these criteria, the maximum MC pressure and NOx emissions maps identified the excluded design configurations, marked as shaded areas.

As expected, increasing spark advance led to an increase in maximum MC pressure, NOx emissions, and ITE, accompanied by a decrease in HC emissions. Decreasing lambda showed negligible variations in maximum MC pressure but resulted in increased NOx and ITE, along with reduced HC emissions.

By examining the ITE map (Fig. 7(c)), specifically within the compliant region, the calibration point maximizing ITE was selected (corresponding to a lambda reduction of 0.05 and baseline spark advance). This case yielded an ITE increase of 0.6% and a reduction in HC emissions of 64.3 ppm.

5. Results and Discussion

This section discusses the results obtained for the various PCC geometries and in-cylinder flow motions. To evaluate the combined impact of PCC design and flow characteristics on ITE, NOx emissions, and HC emissions, the findings from Section 4.2 are presented in Fig. 8. Specifically, the figure plots these metrics as a function of the A/V ratio for all PCC configurations summarized in Table 5. Filled markers denote the designs characterized by an ITE higher than the baseline, alongside HC and NOx emissions levels that are equal to or lower than the baseline (identified as compliant). Conversely, empty markers indicate configurations that fail to meet these optimization criteria (identified as non-compliant). All presented findings refer strictly to the baseline calibration settings.

Fig. 8 demonstrates that, across all in-cylinder flow motions, increasing the PCC A/V ratio led to a reduction in efficiency and NOx emissions, accompanied by an increase in HC emissions, especially at low engine load. This behaviour is attributed to the fact that a higher A/V ratio diminishes the combustion intensity within the PCC (lower peak PCC pressure) and consequently the combustion duration into the MC decreases, as also found experimentally by Shah et al. [17,22].

Across all engine load levels, swirl emerged as the most promising flow motion, providing the greatest benefits in terms of ITE gain and HC emissions reduction. This is attributed to the faster combustion process associated with swirl, as confirmed by Fig. 9, which shows the experimental burn rates comparison for the three flow motions derived from a different engine platform equipped with the same combustion technology. Also in this case, swirl motion allows a more intense and faster combustion process in the main chamber compared to tumble. This phenomenon can be attributed to the swirl's more pronounced and prolonged influence on the flame propagation.

Indeed, these findings align with the 3D-CFD simulations by Khan et al. [26], which validated the effectiveness of swirl motion. They observed that, unlike in quiescent environments where the flame front tends to impinge directly on the cylinder walls, swirl flow generates a more uniform flame expansion with a larger surface area. Being less

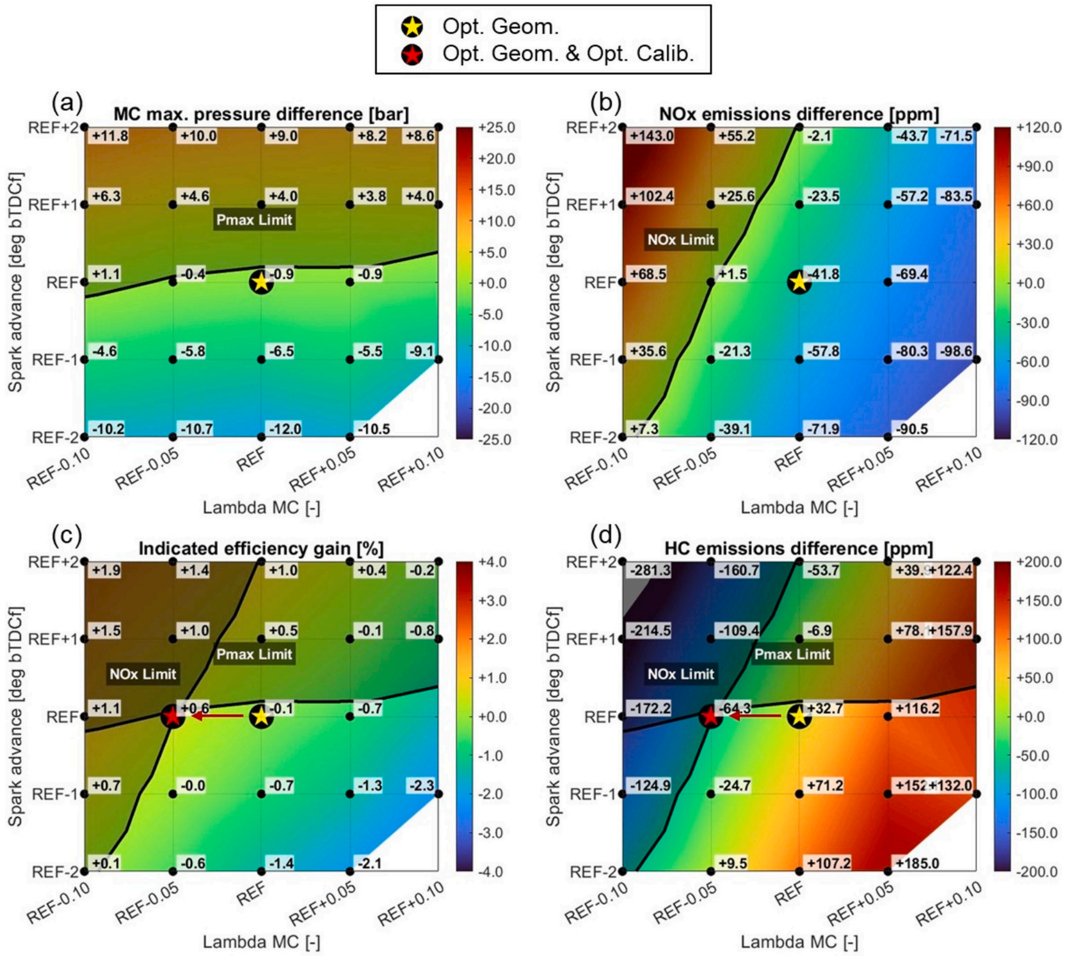

Fig. 7. Optimal lambda and spark advance calibration for quiescent flow, REF number of nozzle holes and 100% Load: (a) Maximum MC pressure, (b) NOx emissions, (c) ITE, (d) HC emissions.

susceptible to quenching, this flow field facilitates rapid and highly efficient combustion, directly translating into increased ITE and reduced HC emissions.

Consequently, this enhanced performance of swirl is accompanied by a significant increase in NOx emissions. However, this penalty can be mitigated by optimizing the lambda and spark advance calibration. While tumble motion yielded lower gains compared to swirl – indicating it as an optimal flow pattern for this specific engine architecture – its results nonetheless demonstrate that introducing any organized in-cylinder flow field offers advantages over a quiescent technology.

The optimal PCC geometry solution appeared to be associated with A/V ratios lower than the baseline, as ITE typically increased with reduced A/V. However, for swirl motion, designs with A/V lower than the reference were not compliant due to excessive NOx formation. Nevertheless, the feasible swirl designs – characterized by an A/V ratio higher than the baseline – exhibited higher efficiency gains compared to tumble designs with lower A/V ratios. Furthermore, the HC emissions reduction offered by swirl is substantial and higher with respect to the other motions.

The simulation outcomes indicated that roughly 85% of the explored geometries yielded non-compliant results. Exploring such a vast parametric space through conventional engine test bench trials would have translated into an unjustifiable expenditure of time and resources, merely to identify and discard these non-optimal designs. Therefore, conventional experimental approaches are intrinsically inefficient when optimizing the ignition technology investigated in this study. Conversely, the proposed simulation platform allows the entire parametric space to be evaluated in approximately 48 hours on a standard commercial personal computer.

Fig. 10 presents the results obtained after section 4.3, displaying the ITE gain and HC emissions reduction outcomes after the optimal calibration of the selected PCC volume and nozzle hole diameter configurations. Specifically, the data covers all combinations of the three numbers of nozzle holes, the three flow motions, and the three engine load levels.

The results indicated that tumble motion yielded higher benefits relative to the quiescent state. Specifically, at full load, the REF-1 hole configuration offered a greater benefit in ITE compared to other hole counts. Regarding HC emissions, tumble was particularly effective at low loads. However, at high load, the advantage over the quiescent is marginal.

Overall, it was evident that swirl provided the greatest benefit compared to the other flow motions under study. At full load, swirl achieved an ITE increase of 1.6%. At mid load, the REF-1 hole configuration yielded the best results, with a 1.3% ITE gain. At low load, the gain was more contained (0.4%) but still outperformed the other flow motions. Despite the limited efficiency gain at low load, swirl demonstrated the most significant HC reduction – particularly for the REF-1 configuration (∼ 600 ppm) – which is clearly higher than both tumble and quiescent results. This substantial reduction in HC emissions was also evident at mid and full load (respectively ∼ 400 ppm and ∼ 300 ppm).

Given that HC emissions are most critical at mid and low load and considering that the REF-1 number of nozzle holes configuration yielded

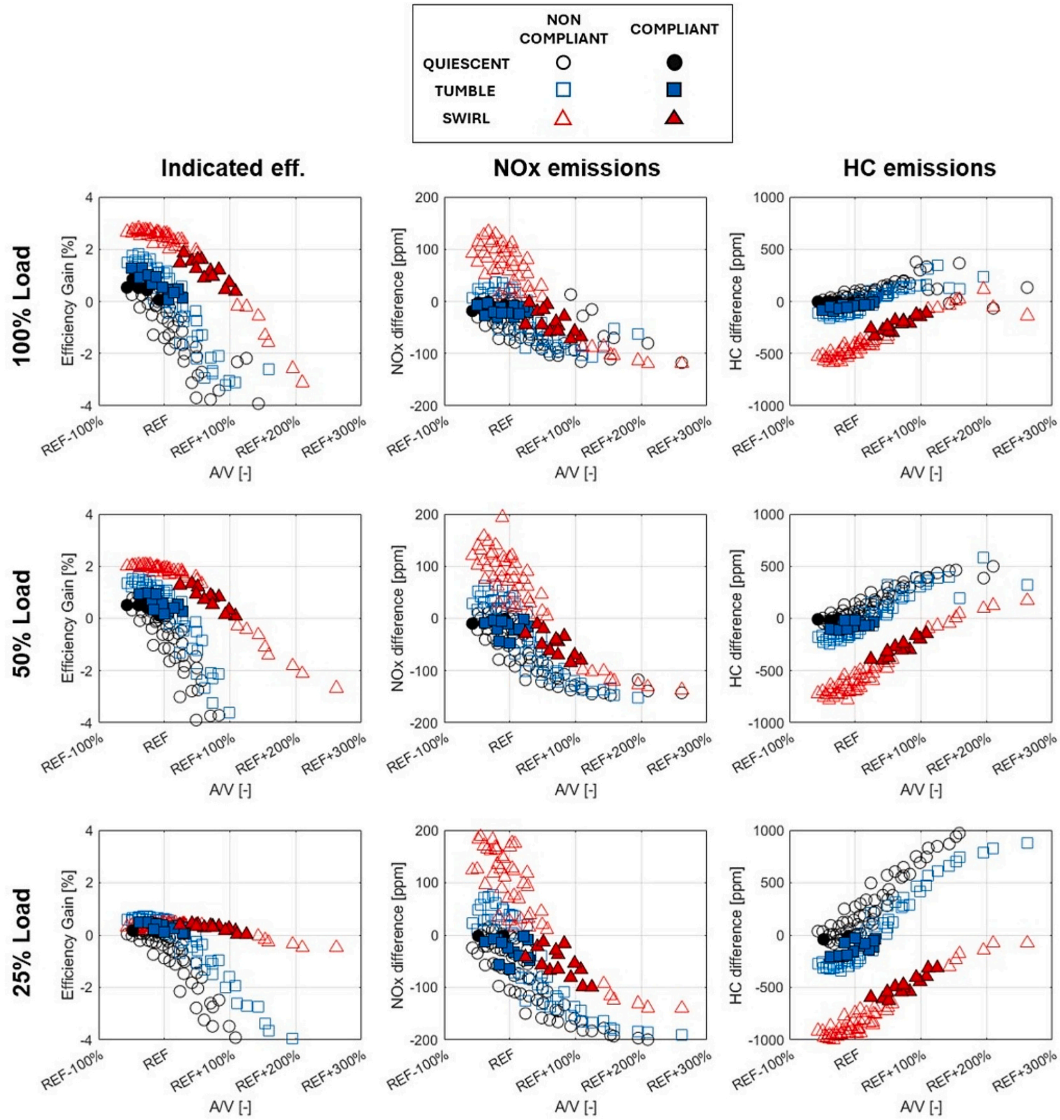

Fig. 8. Impact of PCC design and flow motion on indicated efficiency, NOx emissions, and HC emissions at different load levels – the designs that present an ITE higher than the baseline, alongside HC and NOx emissions levels that are equal to or lower than the baseline, are represented by the filled markers.

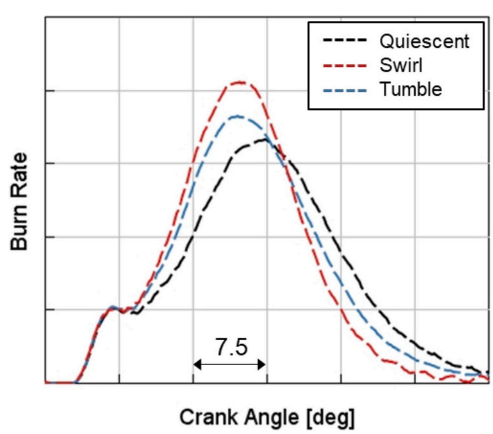

Fig. 9. Experimental burn rate profiles for the quiescent (black), tumble (blue), and swirl (red) flow configurations acquired on a comparable engine platform equipped with the same ignition technology.

the best results in these regimes, the combination of REF-1 and swirl motion was identified as the optimal solution among all investigated designs.

The specific architectures of the identified optimal design are outlined in Table 6, whereas Table 7 highlights the resulting performance gains regarding ITE and HC emissions for the three load levels under study.

In this case, a lower PCC volume and hole diameter, along with an induced swirl motion inside the MC, have shown the best results in terms of performance and emissions formation.

Fig. 11 compares the baseline and optimal pressure traces and HRR generated by the predictive combustion model. The resulting peak PCC pressure was lower due to the A/V ratio increase. Combustion appeared to be slower in its first phase due to the lower intensity of the PCC combustion. The reduction in PCC peak pressure resulted in a lower NOx formation. Simultaneously, the swirl motion shortened the combustion duration, leading to higher ITE and, consequently, lower HC emissions.

The comparison of these results with the experimental data of Fig. 9 reveals that the slower, initial phase of combustion is dictated only by the PCC geometry. Since the experimental traces, obtained using an identical PCC configuration, overlap during this initial phase, it is evident that the early combustion dynamics remain completely uninfluenced by variations in the in-cylinder flow motion. Furthermore,

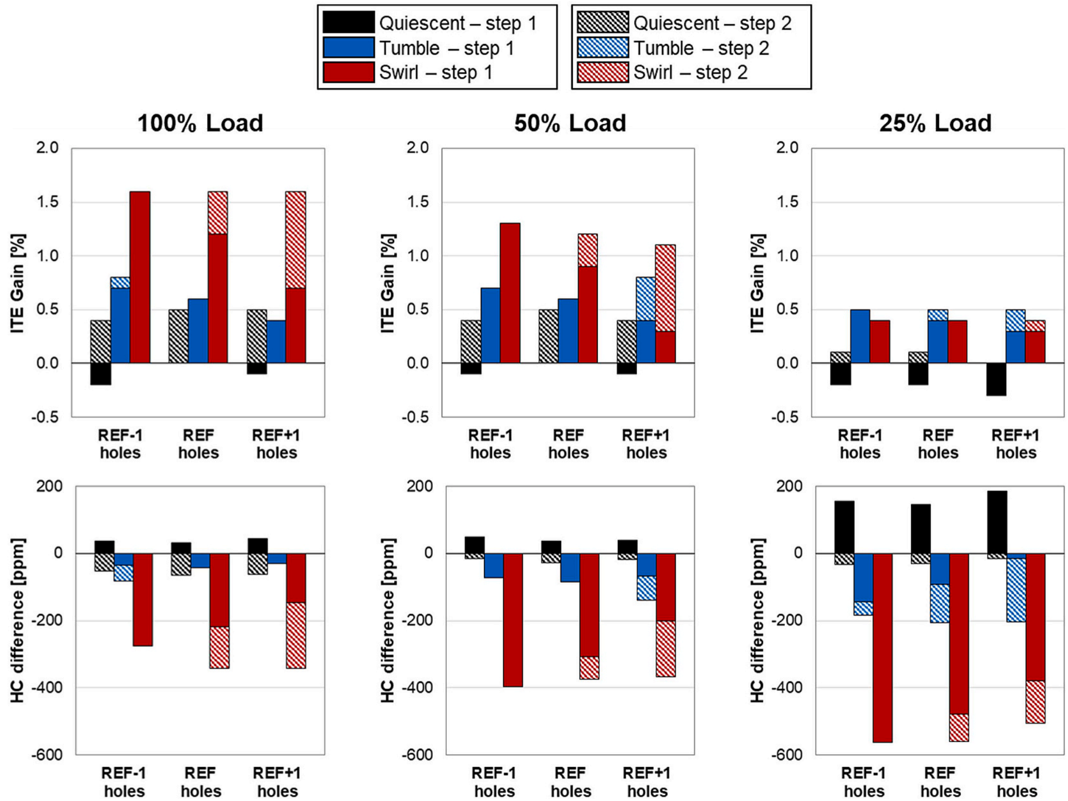

Fig. 10. Impact of in-cylinder flow motion and the number of PCC holes on indicated efficiency gains and HC emission variations. Step 1 and Step 2 denote the results obtained prior to and following engine recalibration, respectively.

Table 6
Optimal flow motion, PCC geometry design and engine calibration

Flow Motion	Swirl
Volume	REF -48%
Hole diameter	REF -28%
Holes number	REF -1
A/V	REF +42%

Table 7
Performance gains regarding ITE and HC emissions for 100%, 50%, and 25% load.

Load	100%	50%	25%
ITE Gain [%]	+1.6	+1.3	+0.4
HC Reduction [ppm]	-276	-396	-562

regarding the subsequent stages of the combustion process, the predicted impact of swirl consistently aligns with the experimental findings.

This study has successfully demonstrated the reliability of the simulation platform, largely due to its high-fidelity combustion and emission models. However, should an experimental corroboration be desired, this tool is able to isolate the optimal design region prior to the experimental campaign. Consequently, the subsequent physical validation will require a drastically reduced number of tests compared to conventional optimization procedures.

6. Conclusions

In conclusion, this study successfully developed a comprehensive 0D/1D-CFD simulation platform within GT-SUITE, integrating predictive combustion, NOx emissions, and HC emissions models. Designed specifically for lean-burn gas engines, the platform proved effective in optimizing PCC geometries and engine calibration across both quiescent and non-quiescent combustion systems. As a digital twin of the real engine, the model demonstrated high sensitivity to both hardware and

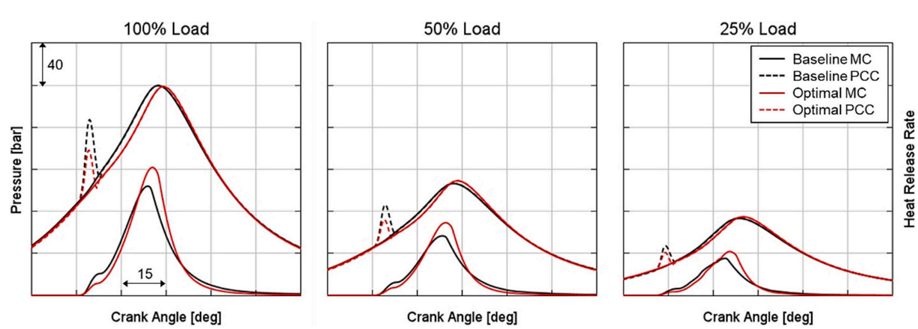

Fig. 11. Baseline and optimal simulation comparison in terms of MC pressure, PCC pressure, and MC HRR over a load variation from 100% to 25%.

calibration variations, enabling robust system-level analysis. The proposed approach emerged as a computationally efficient alternative to 3D-CFD simulations, thus offering a valuable alternative in experimental test-bench requirements. Consequently, this tool provides a viable pathway to decrease time-to-market, development costs, and the carbon footprint associated with the engine design process.

The study presented a dedicated optimization methodology using the developed simulation tool. By systematically evaluating the interactions between PCC geometry, in-cylinder flow motion, and engine calibration, the optimal configuration was determined. This optimization effectively maximized ITE and minimized HC emissions, strictly keeping NOx emissions at or below the baseline levels.

The results indicated that swirl motion outperformed both tumble and quiescent systems, demonstrating superior potential for increasing ITE at full and mid-load due to faster combustion. Furthermore, swirl consistently reduced HC emissions across all load levels, with particularly significant reductions at low load. Although the faster combustion inherently tends to increase NOx, this effect can be effectively mitigated by increasing the PCC A/V ratio to dampen combustion intensity in the PCC. Even with this adjustment to control NOx, the swirl configuration still yielded gains in ITE and reductions in HC emissions.

Regarding the optimal PCC geometry under swirl motion, the study identified that a significant reduction in PCC volume (-48%) and nozzle hole diameter (-28%) – leading to a +42% increase in the A/V ratio – yielded the best overall performance. This configuration achieved a maximum ITE gain of +1.6% (at full load) and a substantial HC reduction of about 600 ppm (at low load). The only required recalibration was a slight mixture enrichment ($\Delta\lambda$-0.05) at low load. While the number of PCC nozzle holes showed a secondary influence, the REF-1 configuration emerged as the most effective solution among the investigated layouts.

The results highlighted that the exploitation of non-quiescent combustion systems for pre-chamber lean-burn large-bore gas engines proved to be a powerful technology. This approach is pivotal for reducing the HC emissions and increasing the engine efficiency, consequently leading to a reduction in fuel consumption and CO_2 emissions.

Acronyms

0D	Zero-Dimensional
1D	One-Dimensional
3D	Three-Dimensional
A/V	Nozzle Area-to-Volume ratio
CFD	Computational Fluid Dynamics
CO_2	Carbon Dioxide
DoE	Design of Experiments
HC	Unburnt Hydrocarbons
ICE	Internal Combustion Engine
ITE	Indicated Thermal Efficiency
L/D	Valve Lift over Diameter ratio
MC	Main Chamber
NOx	Nitrogen Oxides
PCC	Pre-Combustion Chamber
REF	Reference
RMSE	Root Mean Square Error

CRediT authorship contribution statement

Andrea Piano: Writing – review & editing, Visualization, Validation, Supervision, Project administration, Methodology, Investigation, Conceptualization. **Guglielmo Rossi:** Writing – original draft, Visualization, Validation, Software, Methodology, Investigation, Data curation. **Federico Millo:** Resources, Funding acquisition. **Enrica Malfi:** Writing – original draft, Software, Resources. **Vincenzo De Bellis:** Writing – review & editing, Software, Resources. **Francesco Lassandro:** Writing – review & editing, Investigation. **Alessandro Cimarello:** Writing – review & editing, Project administration, Conceptualization. **Jari Hyvönen:** Writing – review & editing, Supervision, Project administration, Conceptualization. **Alberto Cafari:** Writing – review & editing, Validation, Supervision, Project administration, Investigation, Conceptualization.

Declaration of competing interest

The authors declare that they have no known competing financial interests or personal relationships that could have appeared to influence the work reported in this paper.

Data availability

The data that has been used is confidential.

References

[1] Burel F, Taccani R, Zuliani N. Improving sustainability of maritime transport through utilization of Liquefied Natural Gas (LNG) for propulsion. Energy 2013. https://doi.org/10.1016/j.energy.2013.05.002.
[2] Mac Kinnon MA, Brouwer J, Samuelsen S. "The role of natural gas and its infrastructure in mitigating greenhouse gas emissions, improving regional air quality. In: and renewable resource integration". Progress in Energy and Combustion science; 2018. https://doi.org/10.1016/j.pecs.2017.10.002.
[3] Wilson IAG, Staffell I. Rapid fuel switching from coal to natural gas through effective carbon pricing. Nature Energy 2018. https://doi.org/10.1038/s41560-018-0109-0.
[4] Elgohary MM, Seddiek IS, Salem AM. Overview of alternative fuels with emphasis on the potential of liquefied natural gas as future marine fuel. Journal of Engineering for the Maritime Environment 2015. https://doi.org/10.1177/1475090214522778.
[5] Guo M, Song W, Buhain J. Bioenergy and biofuels: History, status, and perspective. Renewable and Sustainable Energy Reviews 2015. https://doi.org/10.1016/j.rser.2014.10.013.
[6] Königsson F, Kuyper J, Stalhammar P, Angstrom HE. The Influence of Crevices on Hydrocarbon Emissions from a Diesel-Methane Dual Fuel Engine. SAE International Journal of Engines 2013. https://doi.org/10.4271/2013-01-0848.
[7] Fasching P, Sprenger F, Eichlseder H. Experimental Optimization of a Small Bore Natural Gas-Diesel Dual Fuel Engine with Direct Fuel Injection. SAE International Journal of Engines 2016. https://doi.org/10.4271/2016-01-0783.
[8] Cho HM, He BQ. Spark ignition natural gas engines-A review. Energy Conversion and Management 2007. https://doi.org/10.1016/j.enconman.2006.05.023.
[9] Dale JD, Checkel MD, Smy PR. Application of high energy ignition systems to engines. Progress in Energy and Combustion Science 1997. https://doi.org/10.1016/S0360-1285(97)00011-7.
[10] Clasen KH, Koopmans L. Investigation of Homogeneous Lean SI Combustion in High Load Operating Conditions. SAE International Journal of Advances and Current Practices in Mobility 2020. https://doi.org/10.4271/2020-01-0959.
[11] Zhu S, Akehurst S, Lewis A, Yuan H. A review of the pre-chamber ignition system applied on future low-carbon spark ignition engines. Renewable and Sustainable Energy Reviews 2022. https://doi.org/10.1016/j.rser.2021.111872.
[12] Toulson E, Schock HJ, Attard WP. A Review of Pre-Chamber Initiated Jet Ignition Combustion Systems. SAE Technical Paper 2010. https://doi.org/10.4271/2010-01-2263.
[13] Rajasegar R, Niki Y, García-Oliver JM, Li Z, Musculus MPB. Fundamental insights on ignition and combustion of natural gas in an active fueled pre-chamber spark-ignition system. Combustion and Flame 2021. https://doi.org/10.1016/j.combustflame.2021.111561.
[14] Olsen DB, Adair JL, Willson BD. Precombustion Chamber Design and Performance Studies for a Large Bore Natural Gas Engine. In: *Proceedings of the ASME 2005 Internal Combustion Engine Division Spring Technical Conference*; 2005. https://doi.org/10.1115/ICES2005-1057.
[15] Takashima Y, Tanaka H, Sako T, Furutani M. Evaluation of Engine Performance and Combustion in Natural Gas Engine with Pre-Chamber Plug under Lean Burn Conditions. SAE International Journal of Engines 2015. https://doi.org/10.4271/2014-32-0103.
[16] Alvarez CEC, Couto GE, Roso VR, Thiriet AB, Valle RM. A review of prechamber ignition systems as lean combustion technology for SI engines. Applied Thermal Engineering 2018. https://doi.org/10.1016/j.applthermaleng.2017.08.118.
[17] Shah A, Tunestal P, Johansson B. Scalability Aspects of Pre-Chamber Ignition in Heavy Duty Natural Gas Engines. SAE Technical Paper 2016. https://doi.org/10.4271/2016-01-0796.
[18] Guo X, Li T, Chen R, Huang S, Zhou X, Wang N, et al. Effects of the nozzle design parameters on turbulent jet development of active pre-chamber. Energy 2024. https://doi.org/10.1016/j.energy.2024.132568.
[19] Hlaing P, Echeverri Marquez M, Bhavani Shankar VS, Cenker E, Ben Houidi M, Johansson B. A Study of Lean Burn Pre-Chamber Concept in a Heavy Duty Engine. SAE Technical Paper 2019. https://doi.org/10.4271/2019-24-0107.
[20] Allison PM, de Oliveira M, Giusti A, Mastorakos E. Pre-chamber ignition mechanism: Experiments and simulations on turbulent jet flame structure. Fuel 2018. https://doi.org/10.1016/j.fuel.2018.05.005.

[21] Gentz G, Thelen B, Gholamisheeri M, Litke P, Brown A, Hoke J, et al. A study of the influence of orifice diameter on a turbulent jet ignition system through combustion visualization and performance characterization in a rapid compression machine. Applied Thermal Engineering 2015. https://doi.org/10.1016/j.applthermaleng.2015.02.026.
[22] Shah A, Tunestal P, Johansson B. Effect of Pre-Chamber Volume and Nozzle Diameter on Pre-Chamber Ignition in Heavy Duty Natural Gas Engines. SAE Technical Paper 2015. https://doi.org/10.4271/2015-01-0867.
[23] Dhotre A, Nyrenstedt G, Rajasegar R, Varma A, Singh S, Northrop W, et al. Exploring the Effects of Varying Pre-Chamber Geometry in a Heavy-Duty Natural Gas Optical Engine under Dilution Conditions. SAE Technical Paper 2025. https://doi.org/10.4271/2025-01-8407.
[24] Piano A, Scalambro A, Millo F, Sementa P, Tornatore C, Catapano F. Numerical analysis on the influence of nozzles geometrical features on the combustion process of passive pre-chamber turbulent jet ignition engine. Transportation Engineering 2025. https://doi.org/10.1016/j.treng.2025.100301.
[25] Millo F, Zanatta M, Scalambro A, Piano A, Accurso F, Pesce FC, et al. Pre-chamber ignition systems for high-speed large-bore gas engine: technology investigation through 3D-CFD analysis. Fuel 2026. https://doi.org/10.1016/j.fuel.2025.138004.
[26] Khan MDT, Kawahara N, Kobashi Y, Yamane I, Hirayama T, Shimizu A, et al. Effect of swirl flow on the main chamber combustion dynamics of methane in a passive pre-chamber spark ignition engine. Fuel 2025. https://doi.org/10.1016/j.fuel.2025.134735.
[27] Liu L, Wu Y, Xiong Q, Liu T. Analysis on flow motion and combustion process in pre-chamber and main chamber for low-speed two-stroke dual-fuel engine. SAE Technical Paper 2019. https://doi.org/10.4271/2019-01-2175.
[28] Zhu J, Wimmer A, Schneßl E, Winter H, Chmela F. Parameter based combustion model for large prechamber gas engines. Journal of Engineering for Gas Turbines and Power 2010. https://doi.org/10.1115/1.4000295.
[29] Bozza F, Teodosio L, Krajnović J, Sjerić M, De Bellis V, Malfi E. Extensive validation of a combustion and pollutant emission model of a pre-chamber engine including different pre-chamber geometries. Fuel 2024. https://doi.org/10.1016/j.fuel.2024.132282.
[30] M. Wenig, K. Roggendorf, and N. Fogla, "Towards Predictive Dual-Fuel Combustion and Prechamber Modeling for Large Two-Stroke Engines in the Scope of 0D/1D Simulation", *CIMAC Congress 2019*, Vancouver, Canada.
[31] Accurso F, Piano A, Millo F, Caputo G, Cimarello A, Cafari A. Numerical Simulation of a Prechamber-Ignited Lean-Burn Gas Engine by means of Predictive Combustion Models. SAE International Journal of Engines 2022. https://doi.org/10.4271/03-16-05-0037.
[32] Mirzaeian M, Millo F, Rolando L. Assessment of the Predictive Capabilities of a Combustion Model for a Modern Downsized Turbocharged SI Engine. SAE technical paper 2016. https://doi.org/10.4271/2016-01-0557.
[33] Millo F, Gullino F, Rolando L. Methodological Approach for 1D Simulation of Port Water Injection for Knock Mitigation in a Turbocharged DISI Engine. Energies 2020. https://doi.org/10.3390/en13174297.
[34] Millo F, Piano A, Rolando L, Accurso F, Gullino F, Roggio S, et al. Synergetic Application of Zero-, One-, and Three-Dimensional Computational Fluid Dynamics Approaches for Hydrogen-Fuelled Spark Ignition Engine Simulation. SAE International Journal of Engines 2022. https://doi.org/10.4271/03-15-04-0030.
[35] Magnussen BF, Hjertager BH. On mathematical modeling of turbulent combustion with special emphasis on soot formation and combustion. Symposium (International) on Combustion 1977. https://doi.org/10.1016/S0082-0784(77)80366-4.
[36] Walther HP, Schlatter S, Wachtmeister G, Boulouchos K. Combustion Models for Lean-Burn Gas Engines with Pilot Injection. MTZ Worldwide 2012. https://doi.org/10.1365/s38313-012-0144-3.
[37] M. Wenig, and K. Roggendorf, "Development of a Predictive Dual-Fuel Combustion and Prechamber Model for Large Two-Stroke Engines Within a Fast 0D/1D-Simulation Environment", *The Working Process of the Internal Combustion Engine Conference 2019,* Graz, Austria.
[38] Millo F, Accurso F, Piano A, Fogla N, Caputo G, Cafari A, et al. Development and Validation of a Multi-zone Predictive Combustion Model for Large-Bore Dual-Fuel Engines. SAE International Journal of Engines 2022. https://doi.org/10.4271/03-15-05-0038.
[39] Narayanaswamy K, Pepiot P, Pitsch H. A chemical mechanism for low to high temperature oxidation of n-dodecane as a component of transportation fuel surrogates. Combustion and Flame 2014. https://doi.org/10.1016/j.combustflame.2013.10.012.
[40] Kobayashi H. Experimental study of high-pressure turbulent premixed flames. Experimental Thermal and Fluid Science 2002. https://doi.org/10.1016/S0894-1777(02)00149-8.
[41] Fogla N, Bybee M, Mirzaeian M, Millo F, Wahiduzzaman S. Development of a K-k-ε phenomenological model to predict in-cylinder turbulence. SAE International Journal of Engines 2017. https://doi.org/10.4271/2017-01-0542.
[42] Lavole GA, Heywood JB, Keck JC. Experimental and theoretical study of nitric oxide formation in internal combustion engines. Combustion Science and Technology 1970. https://doi.org/10.1080/00102206908952211.
[43] Namazian M, Heywood JB. Flow in the Piston-Cylinder-Ring Crevices of a Spark-Ignition Engine: Effect on Hydrocarbon Emissions, Efficiency and Power. SAE Technical Paper 2018. https://doi.org/10.4271/820088.
[44] Boust B, Sotton J, Labuda SA, Bellenoue M. A thermal formulation for single-wall quenching of transient laminar flames. Combustion and Flame 2007. https://doi.org/10.1016/j.combustflame.2006.12.019.
[45] Malfi E, De Bellis V, Bozza F, Cafari A, Caputo G, Hyvönen J. A phenomenological model for the description of unburned hydrocarbons emission in ultra-lean engines. International Journal of Engine Research 2022. https://doi.org/10.1177/14680874211005063.
[46] De Bellis V, Malfi E, De Felice M, Lanotte A, Cafari A, Caputo G, et al. A comprehensive phenomenological model for unburned fuel emission simulation applied to natural gas engines. Fuel 2024. https://doi.org/10.1016/j.fuel.2024.131440.
[47] Malfi E, Esposito S, De Felice M, Pitsch H, Pischinger S, De Bellis V. Phenomenological model for unburned hydrocarbon emissions from spark-ignition, pre-chamber, and dual-fuel internal combustion engines. International Journal of Engine Research 2024. https://doi.org/10.1177/14680874241255157.
[48] Esposito S, Malfi E, De Felice M, Golc D, Beeckmann J, Pitsch H, et al. Methanol fuelling of a spark-ignition engine: Experiments and 0D/1D predictive modelling for combustion, performance, and emissions. Fuel 2025. https://doi.org/10.1016/j.fuel.2025.134657.
[49] Jensen TK, Schramm J. The Role of Post Flame Oxidation on the UHC Emission for Combustion of Natural Gas and Hydrogen Containing Fuels. SAE Technical Paper 2003. https://doi.org/10.4271/2003-01-1775.
[50] Kuppa K, Nguyen HD, Goldmann A, Korb B, Wachtmeister G, Dinkelacker F. Numerical modelling of unburned hydrocarbon emissions in gas engines with varied fuels. Fuel 2019. https://doi.org/10.1016/j.fuel.2019.05.115.
[51] Lawrence CKW, Dryer FL. Simplified Reaction Mechanisms for the Oxidation of Hydrocarbon Fuels in Flames. Combustion Science and Technology 1981. https://doi.org/10.1080/00102208108946970.